INT. J. REMOTE SENSING, 10 AUGUST, 2004,
VOL. 25, NO. 15, 2903–2917

Taylor & Francis
Taylor & Francis Group

Aerosol optical depth spatio-temporal characterization over the Canadian BOREAS domain

C. BERTRAND*

Royal Meteorological Institute of Belgium, Department of Observations, Section Remote Sensing from Space, Avenue Circulaire 3, B-1180 Brussels, Belgium; e-mail: Cedric.Bertrand@oma.be

and A. ROYER

Centre d'Applications et de Recherches en Télédétection (CARTEL), Université de Sherbrooke, Sherbrooke, Québec, J1K 2R1, Canada; e-mail: alain.royer@usherbrooke.ca

(*Received 27 March 2003; in final form 27 August 2003*)

Abstract. A complete set of Advanced Very High Resolution Radiometer (AVHRR) data (75 images) is used to retrieve aerosol optical depth (AOD) over dense vegetation and over lake water in the visible AVHRR channel. The present approach for remote sensing of aerosols from the National Oceanic and Atmospheric Administration (NOAA)-11 AVHRR sensor is based on the detection of atmospherically dominated signals over dark surface covers such as dense dark vegetation (DDV). Such targets were identified using the reflective portion of the middle-wave AVHRR channel 3 signal. When a fixed DDV surface reflectance is subtracted from the observed reflectance after correction for all other atmospheric effects, the remaining part, which is due to aerosols, is inverted to derive aerosol optical thickness using a look-up table (LUT) similar to that used in water surface inversion. The algorithm was applied to the daily afternoon NOAA-11 AVHRR (1 km × 1 km) data acquired from the end of May to mid-August 1994 over the Canadian 1000 km × 1000 km Boreal Ecosystem Atmosphere Study (BOREAS) domain. A validation analysis using five ground-based Sun photometers within the studied area shows the good performance of the retrieval algorithm. The approach allows detailed analysis of the AOD spatio-temporal behaviour at the regional scale useful for climate and transport model validation.

1. Introduction

Atmospheric aerosols are of great importance because of their impacts on human health, visibility, continental and maritime ecosystems, or the Earth's climate, requiring dedicated monitoring of their concentrations and properties at both the regional and global scales. Towards this objective, satellite observations of aerosols are playing an increasing role (Kaufman *et al.* 2002). The last decade has shown major improvement in tropospheric aerosol remote sensing capabilities, with

*Corresponding author.

International Journal of Remote Sensing
ISSN 0143-1161 print/ISSN 1366-5901 online © 2004 Taylor & Francis Ltd
http://www.tandf.co.uk/journals
DOI: 10.1080/01431160310001632657

spacecraft now carrying sensors especially devoted to this application (e.g. the Polarization and Directionality of the Earth's Reflectances (POLDER) instrument, the Moderate-resolution Imaging Spectroradiometer (MODIS), the Multi-angle Imaging Spectroradiometer (MISR), and the Advanced Along-track Scanning Radiometer (AATSR)). However, while these instruments specifically designed for aerosol retrievals now enable quantitative aerosol observations, only data originating from airborne instruments not explicitly designed for this application present long-term continuous measurement (which are particularly useful to evaluate the seasonal variations in aerosol concentrations and properties in numerical models) which the newest satellite sensors cannot provide for 20 years.

In that context, only aerosol products from the Total Ozone Mapping Spectrometer (TOMS) and from the Advanced Very High Resolution Radiometer (AVHRR) data turn out to be useful because of their long temporal series. TOMS, an ultraviolet scanning monochromator, was initially launched in 1978 on Nimbus-7. It is especially sensitive to absorbing aerosol particles, both over land and ocean, but is hampered in doing quantitative aerosol analysis by its large footprint (field of view of 50 km), which makes sub-pixel cloud contamination by far its largest problem (Torres *et al.* 1998). The other long-term sensor, AVHRR (long-term dataset since 1979), is a five-band cross-track scanning radiometer flown on National Oceanic and Atmospheric Administration (NOAA) polar orbiting satellites since 1978. The current version of the AVHRR was first launched in an afternoon orbit on NOAA-7 in 1981. Since then, AVHRR sensors have flown on three more afternoon NOAA satellites with the only gap in coverage from September 1994 to February 1995 when NOAA-11 AVHRR failed. The global afternoon coverage of nearly 20 years provides a significant opportunity to understand a long-term distribution of aerosols. Despite the absence of on-board calibration of the visible bands, research toward this end has begun and is in majority directed towards retrieving the most accurate aerosol information over the ocean (e.g. Higurashi *et al.* 2000, Stowe *et al.* 2002). Recently, Knapp and Stowe (2002) highlighted the potential for retrieving aerosol optical depth (AOD) also over land from AVHRR, particularly over a dark background.

The purpose of our research effort is to show that data originating from the AVHRR instrument are well suited for providing aerosol optical depth spatio-temporal information at more detailed scale in western Canada. The present approach is based on detection of aerosol over dark surface such as the dark dense vegetation (DDV) targets using the reflective part of the AVHRR 3.55–3.93 μm channel. The method is applied to NOAA-11 AVHRR (1 km $\times$ 1 km) data acquired from the end of May to mid-August 1994 over the Boreal Ecosystem Atmosphere Study (BOREAS) super-site. It is a 1000 km $\times$ 1000 km domain straddling the Canadian boreal forest (see Sellers *et al.* 1995).

2. Data processing and dark surface identification

2.1. *Data pre-processing*

The daily afternoon NOAA-11 AVHRR data from 24 May to 14 August 1994 acquired from Environment Canada's high-resolution picture transmission (HRPT) site (Edmonton, Canada), were processed in order to produce calibrated, cloud-screened and co-registrated (1 km polar stereographic projection) images over the 1000 km $\times$ 1000 km BOREAS site (Bussières *et al.* 2002). Orbits were selected to have the smallest possible satellite viewing angle for the analysis. At-sensor visible reflectances in channel 1 (0.58–0.68 μm), near-infrared (NIR) reflectances in channel

2 (0.725–1.10 μm) and radiances in channel 3 (3.55–3.93 μm) were generated according to the NOAA calibration procedures taking into account time-dependent gain and offset coefficients. Brightness temperatures in channels 4 (10.3–11.3 μm) and 5 (11.5–12.5 μm) used here to detect clouds and to derive reflectivity in channel 3 (see § 2.2) were calibrated using in-orbit time-varying gain and offset coefficients and corrected for nonlinearity. The land surface temperatures were then derived by applying the split window approach (Sobrino *et al.* 1991) for atmospheric correction.

The presence of cloud was determined by examining the properties of AVHRR channels 2 and 4. Each scene was examined individually to determine the combination of thresholds in AVHRR NIR reflectance (channel 2) and brightness temperature (channel 4) that provide the best discrimination between land and clouds. For each AVHRR pixel in a scene, if the NIR reflectance exceeded 25% and if the brightness temperature was less than a scene-dependent threshold ranging from 268–276 K, the pixel was classified as cloudy. Note that thin cirrus clouds are sometimes not eliminated (e.g. Bussières 2002, Bussières *et al.* 2002) when applying such a cloud screening procedure. This residual cloud contamination is discussed later.

The last processing step was to characterize the atmospheric conditions for each scene, and in particular the water vapour content variations. Due to the large area analysed, sparse weather station measurements over the BOREAS site cannot be used for the overall area. To overcome this difficulty, the gridded water vapour content from the Canadian operational weather forecasting regional finite element model (RFE) (Mailhot *et al.* 1995) has been used. Note that the RFE gridded water vapour content data were calibrated against synchroneous Sun photometer water vapour measurements during the same period (see Halthore *et al.* 1997) as an unexplained bias has been observed between the model and calibrated ground-based measurements. This allowed us to estimate for each pixel in a scene the water vapour content taken as input for atmospheric correction of channels 2, 3, 4 and 5 (water vapour transmission and split window algorithm).

2.2. *Estimation of the reflectivity signature at 3.75 μm from AVHRR data*

Remote sensing of aerosol over land is complicated because reflection of sunlight by the variable surface cover can be confused with the backscattering by the aerosol layer. The lower the surface reflectance, the lower is the effect of uncertainty in the surface properties on remote sensing of aerosols using radiance. Kaufman and Sendra (1988) suggested to detect dark targets by using the vegetation index (the Normalized Difference Vegetation Index (NDVI) composed of radiances in the red and NIR channels) measured at the top of the atmosphere (TOA). Determination of dark pixels using the vegetation index is, however, affected by the sensitivity of the vegetation index itself to aerosols. To avoid this feedback loop the method was applied only to images for which it was known *a priori* that dense vegetation pixels were present in the image (Soufflet *et al.* 1997). An alternative technique is the use of longer wavelengths that are less sensitive to the aerosol scattering while still sensitive to the surface characteristics to locate dark pixels. As an example, the use of the 3.75 μm AVHRR channel allows to alleviate the restriction associated with the vegetation index when detecting dense vegetation (Holben *et al.* 1992, Kaufman and Remer 1994). The advantage of this long wavelength is that it is not affected by accumulation mode aerosol, e.g. sulphates

and organic particles (Kaufman and Remer 1994), though it could be affected by dust (Ackerman 1989). The measured reflectance in this channel can be used to detect forested or dense vegetation pixels that are the darkest pixels over land. In addition, Kaufman and Remer (1994) emphasized that the apparent reflectance in the 3.75 μm AVHRR channel is well correlated with the reflectance in channel 1 (0.64 μm).* However, as the 3.75 μm is affected by emitted radiation and atmospheric absorption, the determination of the presence of the dark pixels in the red (0.64 μm) AVHRR channel using their reflectivity signature at 3.75 μm therefore requires to correct the 3.75 μm channel from thermal emission and water vapour absorption before processing.

Assuming that the effect of aerosols in the thermal range (channels 3, 4 and 5 of AVHRR) is negligible, we used the method developed by Roger and Vermote (1998) to retrieve the reflectivity signature at 3.75 μm from AVHRR data. This method consists of estimating the part of the signal in channel 3 due to emitted radiation and subtracting it from the total signal to deduce the reflective component by dividing the remaining signal component by atmospheric transmission and solar irradiance. The thermal component in channel 3 is expressed as a second-degree polynomial of the observed signals from channels 4 and 5 and emissivities in 4 and 5. Over clear lake (no aerosol, no cloud) the emissivities in channels 3, 4 and 5 are modelled as a function of the agitation state of the surface (Masuda *et al.* 1988). Over land, as the surface emissivities in channels 3, 4 and 5 are unknown and vary with cover type (Van de Griend and Owe 1993), the emissivity in the infrared channels is taken as a function of surface greenness and assumed to be equal to a linear function of the logarithm of NDVI (Van de Griend and Owe 1993).

The water vapour transmittance is computed as a double exponential function of the air mass and the water vapour amount, U_{H_2O}, according to the formulation provided by Roger and Vermote (1998). The other atmospheric gases interacting primarily in the range of wavelengths over channel 3 are O_3, H_2O, CH_4, N_2O, N_2 and CO_2. Their transmittances are assessed by a second degree polynomial function in the air mass (see Roger and Vermote 1998 for further information).

Finally, the 'dark targets' are selected over land by considering pixels whose reflectance at 3.75 μm is between 0–0.05 and whose NDVI is greater than zero (to eliminate waterbodies). When identified in the image, we assigned a surface reflectance value of respectively 0.025 and 0.015 for the dark surface pixels over land and lake in AVHRR channel 1. These surface reflectance values appear as those that minimize the difference between the retrieved and measured AOD (see discussion in § 4). For the boreal evergreen coniferous forest they can be assumed to be relatively constant and homogeneous over the summer season even if understorey vegetation may slightly change reflectances (Cihlar *et al.* 1997).

3. Aerosol optical depth retrieval algorithm

Remote sensing of aerosol stems from the relationship between the measured radiance at the TOA and the surface bidirectional reflectance properties. Therefore for a given atmospheric condition and assuming that the ground is Lambertian above dark pixels, the AOD retrieval consists of an iterative search for the

*The presence of vegetation decreases the reflectivity in the visible channels due to chlorophyll absorption and in the mid-infrared channels due to absorption by liquid water associated with the plant. Wet soil has a lower reflectance in the visible channels due to light-trapping capability and in the 3.75 μm channel due to liquid water absorption.

atmospherically corrected reflectance value, ρ_{ac}, that produces a reflectance (or radiance) equal to the apparent reflectance (or apparent radiance) recorded by the sensor at the TOA, ρ_i^*:

$$\rho_{ac}(\mu_s, \mu_v, \phi) = \frac{\rho'_{ac}}{1 + \rho'_{ac} S} \tag{1}$$

where S is the spherical albedo of the atmosphere, and

$$\rho'_{ac} = \frac{\frac{\rho_i^*(\mu_s, \mu_v, \phi)}{T_g} \rho_a(\mu_s, \mu_v, \phi)}{T(\mu_s) T(\mu_v)}$$

where ρ_i^* is the input parameter and where all the other parameters (the gaseous transmission, T_g; the path radiance, $\rho_a(\mu_s, \mu_v, \phi)$; and the total upward, $T(\mu_v)$, and downward, $T(\mu_s)$, transmittance) are computed in the atmospheric conditions described by the user.

The gaseous transmission, T_g, accounts for the contribution from O_3, O_2 and H_2O. Similarly to Roger and Vermote (1998) who expressed the gaseous transmittance in the AVHRR channel 3 as a function of the air mass, M, and the gases' concentrations, the contribution of O_3, O_2 and H_2O have been parametrized by running the 6S radiative transfer model (Vermote *et al.* 1997a) to determine the gaseous transmission for each gas in the AVHRR channel 1 for a range of total amount of gas and a range of viewing angles. The following analytical equation has been considered for the ozone transmission:

$$T_g(O_3, M) = \frac{1}{1 + a_1 (M U_{O_3})^{b_1}} \tag{2}$$

where U_{O_3}, the total ozone amount (cm atm^{-1}), is taken from the gridded ozone concentration climatology of London *et al.* (1976). The constants a_1 and b_1 are listed in table 1.

The formula adopted for oxygen is:

$$T_g(O_2, M) = \exp\left(-a_2 M^{b_2}\right) \tag{3}$$

where the O_2 concentration is considered to be invariant. The two constants a_2 and b_2 are provided in table 1.

The analytical formulation for the water vapour transmission is:

$$T_g(H_2O, M) = \exp\left[a_3 + b_3 \ln(M U_{H_2O}) + c_3 \ln^2(M U_{H_2O})\right] \tag{4}$$

where U_{H_2O}, the total precipitable water, is the corrected water content originating from the RFE model. The values of the three constants a_3, b_3 and c_3 are provided in table 1.

Using the single scattering approximation, the path radiance, $\rho_a(\mu_s, \mu_v, \phi)$, is proportional to the AOD, τ_a, the aerosol scattering phase function, $P_a(\mu_s, \mu_v, \phi)$,

Table 1. Constants used in the atmospheric correction procedure (gaseous transmission) of the AVHRR channel 1 (equations (3)–(5)) (derived from Vermote *et al.* 1997a—6S model).

$i=$	a_i	b_i	c_i
1	0.08717736	1.036156088	
2	0.00217670	0.551440000	
3	−0.0099062	0.004764100	−0.0059961

and the single-scattering albedo, ω_o, we can write:

$$\rho_a(\mu_s, \mu_v, \phi) = \rho_r(\mu_s, \mu_v, \phi) + \frac{\omega_a \tau_a P_a(\mu_s, \mu_v, \phi)}{4\mu_s \mu_v} \quad (5)$$

where $\rho_r(\mu_s, \mu_v, \phi)$ is the path radiance due to molecular scattering, μ_s and μ_v the cosines of solar zenith angle and view angle respectively, and ϕ the relative azimuth angle. In order to save computer resources but maintain a good accuracy, the Rayleigh reflectance, transmission and spherical albedo computation is based on analytical formulation developed by Vermote and Tanré (1992). This approach uses the quasi-isotropic behaviour of molecular scattering to develop an analytical expression of the atmospheric reflectance and uses a two-stream method corresponding to the Eddington approximation to describe the transmission function and compute the spherical albedo.

The total transmittance can be divided into a direct and a diffuse part such that:

$$T(\mu_s) = e^{-\tau/\mu_s} + t_d(\mu_s) \quad (6)$$

and likewise for $T(\mu_v)$, where τ is the total optical thickness and t_d the diffuse transmittance. The quantities $\rho_a(\mu_s, \mu_v, \phi)$, t_d and S are functions of the optical thickness, single-scattering albedo, and phase function of the scatterers and absorbers in the atmosphere. They are provided by the use of an aerosol model. According to the geographical location of the BOREAS super-site we assigned the aerosol model to be a continental aerosol model (WCP112; World Meteorological Organization (WMO) 1986). It is worth pointing out that the use of such an aerosol model does not necessarily produce accurate representations of the aerosol size distribution or aerosol absorption, especially in the case of aerosols generated by forest fires.

As our algorithm is not appropriate to allow meaningful AOD retrievals in the Sun glint contaminated regions, measurement of radiances affected by Sun glint have been masked out. Namely, the normalized Sun glint radiance is computed based on the assumption that the wind-ruffled lake surface consists of a collection of individual facets obeying the slope statistics derived by Cox and Munk (1954). As an approximation, the normalized Sun glint radiance is computed with a further assumption that the wind-ruffled surface slope distribution is independent of the wind direction and by considering an invariant lake surface wind speed of $7.5\,\mathrm{m\,s^{-1}}$. A mask is applied to areas where normalized glint radiance is greater than a predetermined threshold (here taken to be 0.005) and the AOD retrieval algorithm is not applied.

Finally, since it is computationally prohibitive to run a radiative transfer model for every dark pixel in the image in order to compute $\rho_a(\mu_s, \mu_v, \phi)$, t_d and S, the AOD is retrieved using a look-up table (LUT) that relates a Lambertian surface reflectance to the recorded radiance as a function of the optical depth and the viewing and illumination geometry. The LUT computations were performed by running the 6S code (Vermote *et al.* 1997a) for 73 relative azimuth angles starting at 0° with a step of 2.5°, 22 solar and view zenith angles starting at 2.48° with a step of 3.71°, and 10 AOD values varying from 0.05 to 2. Similar LUTs are described in Fraser *et al.* (1992) who reported that errors in the derived surface reflectance resulting from interpolation between entries in the LUT are large only when either Sun angle or view angle are extreme ($>70^\circ$). Uncertainty caused by interpolation from the LUT was found to cause errors in the corrected reflectance of less than 0.005 for surface reflectance of 0.05. The Lambertian approximation error may be

the most important error in the atmospheric correction process. Nevertheless, Lee and Kaufman (1986) have shown that the error resulting from this approximation is small for dark surfaces used to derive the aerosol path radiance and optical depth. More specifically, these authors have shown that the error is small outside the backscattering direction (hotspot) and expected to be larger at short wavelengths and with increasing solar zenith angle.

4. Results

The algorithm was applied to NOAA-11 AVHRR data acquired from 24 May to 14 August 1994 over the Canadian BOREAS super-site. An evaluation of the resulting optical depths was undertaken by comparing them to ground measurements obtained by Cimel Sun photometers. Indeed, as illustrated in figures 3 and 4, five AEROCAN sites (the Canadian subnetwork of the federated Aerosol Robotic Network (AERONET)) are present in the BOREAS domain. Two of them are located in Saskatchewan, namely at Waskesiu and in the Southern Study Area (SSA_YJP_BOREAS) experiment site, the three other locations (Thompson, Flin-Flon and the Northern Study Area (NSA_YJP_BOREAS experiment site)) being in Manitoba. AEROCAN Sun photometer data are collected at these sites simultaneously with the satellite data.

It is worth pointing out that whereas AVHRR achieves a complete coverage of the BOREAS domain once a day, Sun photometer retrievals occur several times a day, but only over individual instrumented locations. AEROCAN AOD data are acquired at 15-min intervals. Therefore, it is necessary to compare spatially averaged AVHRR pixels with synchronous AEROCAN measurements for many reasons. First, the parameter value in an image pixel represents a spatial average over the pixel surface (an area of $1\,\text{km} \times 1\,\text{km}$ for AVHRR-derived AOD), and cannot be justifiably equated with a point value measured with a Sun photometer. Secondly, even if the pixel is small enough to represent a point, it is extremely unlikely that it would represent the same conditions as a Sun photometer point data, since their observation axes are different and the atmosphere is constantly in motion. Again, clouds may obscure an AVHRR pixel directly over a Sun photometer site, but may not affect nearby pixels. In the same way, times of Sun photometer measurements seldom coincide exactly with AVHRR overpass times, the closest pair being often larger than 5 min apart. With cloud contamination and consequent data filtering, the shortest time difference can stretch even longer. Therefore, to validate our retrieval scheme, we have compared spatially averaged AOD values from AVHRR (the mean of maximum 100 AVHRR pixels in a square box of $10\,\text{km} \times 10\,\text{km}$ centred over the Sun photometer sites) with the closest Sun photometer AOD measurements within ± 30 min of AVHRR overpasses. Finally, using the Angström coefficient computed from CIMEL measurements at 670 nm and 440 nm to describe the AOD spectral behaviour (see Bokoye *et al.* 2001), we derived CIMEL AOD values at 640 nm.

Comparisons of retrieved AVHRR channel 1 optical depth using a continental aerosol model versus the measured optical depth are provided in figure 1 and show good agreement. Also highlighted in this figure is a net overestimation which occurs in some retrieved AOD values with regard to ground measurements. For each of the four AOD overestimations identified in figure 1, we provide in figure 2 the full day Sun photometer records. Figure 2 shows that the satellite samplings occurred during time periods for which no Sun photometer measurements were reported due to a cloudy atmosphere above the AEROCAN sites. Figure 2(*a*) clearly indicates

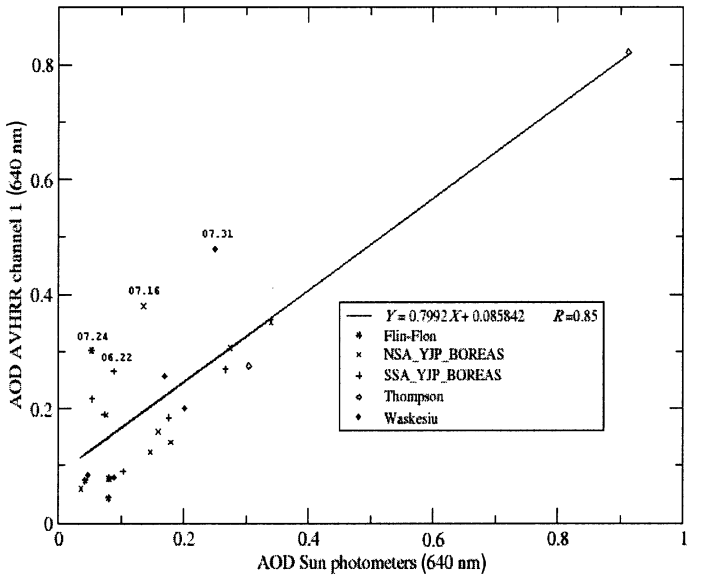

Figure 1. Retrieval of optical depth in AVHRR channel 1 using the 'dark targets' approach (reflectivity signature at 3.75 μm is used for 'dark targets' detection) compared with Sun photometer data.

that the overestimation in the retrieved AOD results from cloud contamination. Therefore it illustrates the failure of the cloud screening procedure based on brightness temperature thresholds (Derrien *et al.* 1993, Jones *et al.* 1996) applied during the data pre-processing in the detection of thin clouds.

Another difficulty which appears in addition to the cloud contamination when comparing the retrieved with the measured AOD value is the fact that, as in Vermote *et al.* (1997b), the AOD is retrieved from an averaged 'dark target' reflectance in channel 1 computed on a $10\,\text{km} \times 10\,\text{km}$ area around the Sun photometer (note that Vermote *et al.* 1997b considered a $50\,\text{km} \times 50\,\text{km}$ area around the Sun photometer). The averaged reflectance can therefore potentially be contaminated by undetected cloudy pixel(s) in the vicinity of the AEROCAN site while at the same time the sky was free of clouds above the CIMEL instrument. Such a possibility explains why the algorithm overestimated the AOD value reported in figure 2(*d*) while the gap between the satellite sampling and the closest Waskesiu ground measurement on 31 July was less than 5 min. Removing these four cloudy contaminated AOD values allows to increase the correlation coefficient between retrieved and measured AOD values up to 0.95 (RMSE = 0.058; note that prior to this correction, RMSE = 0.102).

On the other hand, the slight underestimation reported in figure 1 for the high AOD Thompson value illustrates the impact of an error on the aerosol model, i.e. by correcting with a continental model when the actual aerosol was smoke (biomass burning) since these models have different phase functions, single scattering albedos and spectral dependence of extinction coefficients. Indeed such an AOD value is clearly associated with the occurrence of a forest fire (Li *et al.* 2000, O'Neill *et al.* 2002); however, we have only considered a continental aerosol model when computing the path radiance, the spherical albedo and the diffuse transmittance. As an example, Fraser *et al.* (1992) reported that uncertainty in the input aerosol phase

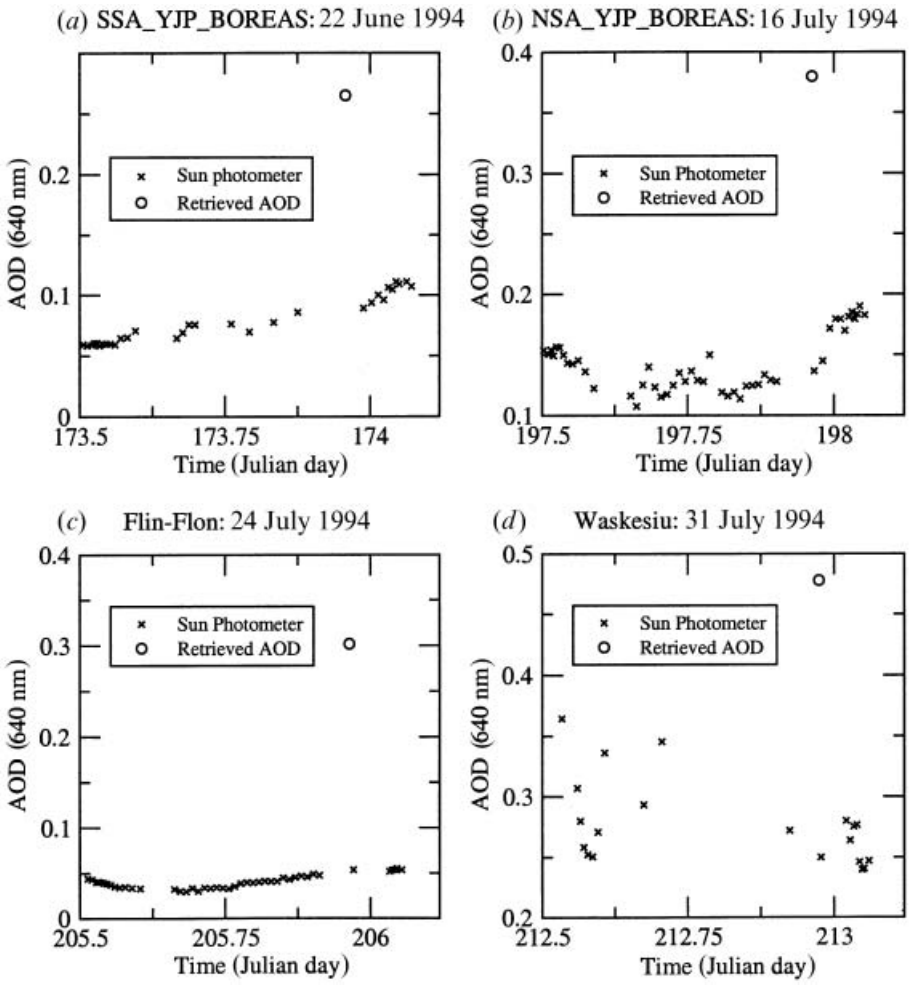

Figure 2. Examples of problematic temporal mismatching when comparing aerosol optical depth from AVHRR channel 1 retrieval with Sun photometer data.

function can cause uncertainty in the correction by as much as 0.02 in reflectance units for a surface reflection of 0.05. By contrast, uncertainty in the input aerosol single scattering parameter causes smaller uncertainties, less than 0.005 (Vermote and Vermeulen 1999).

Additional confidence in our AOD retrieval procedure relies on the continuity that appears between AOD values retrieved above the boreal forest and above the lake surfaces. Moreover, these AOD values are well in accordance with Li *et al.* (1996) and Loechel *et al.* (1997). Such a smooth transition in the AOD values retrieved above these two surface types is well illustrated in figure 3 where the AOD patterns retrieved above Lake Winnipeg (lower right part of the image) are well in agreement with the patterns retrieved above the neighbouring DDV surfaces. It is worth pointing out that while Soufflet *et al.* (1997) assumed a surface reflectance value of respectively 0.023 and 0.013 for dark surface pixels over land and lake in the AVHRR channel 1 to perform their inversion procedure, we assigned a reflectance value of 0.025 for the DDV surfaces and 0.015 for the lake surfaces in

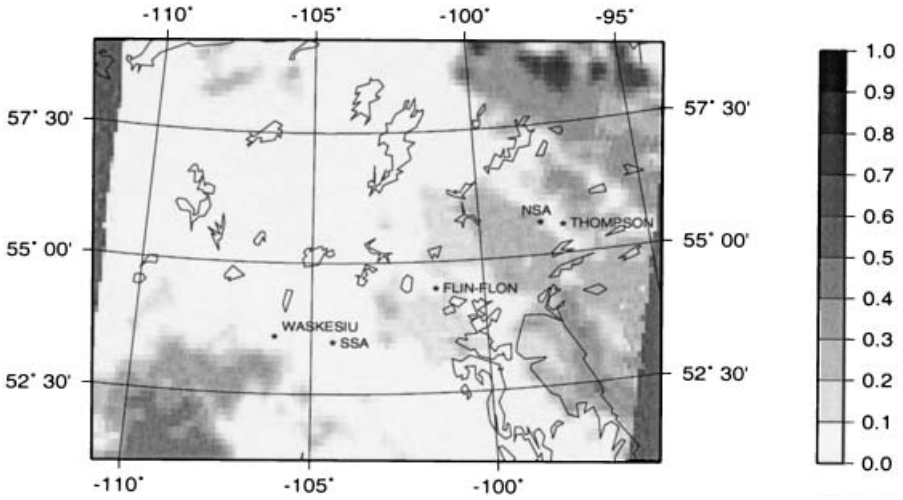

Figure 3. Aerosol optical depth derived from cloud-free NOAA-11 AVHRR channel 1 reflectance data over the BOREAS super-site on 7 July 1994 (Julian day 190).

this channel. These two values give the best continuity between the AOD fields retrieved above DDV surfaces and lake surfaces, among the different surface reflectance values we have considered in the inversion scheme (namely 0.023, 0.025 and 0.028 for dark land, and 0.013 and 0.015 for water surface). In addition a surface reflectance value of 0.025 for the dark surface pixels over land in AVHRR channel 1 accounts for the better correlation coefficient when comparing the retrieved AOD values with the five AEROCAN Sun photometer data.

Two animations (available at ftp://gerb.oma.be/cedric/) provide the time evolution of the AOD derived from NOAA-11 AVHRR channel 1 reflectance data over the BOREAS domain from the end of May to mid-August 1994. The file 'AOD-BOREAS94_B.gif' displays the direct result of the AOD retrieval scheme on

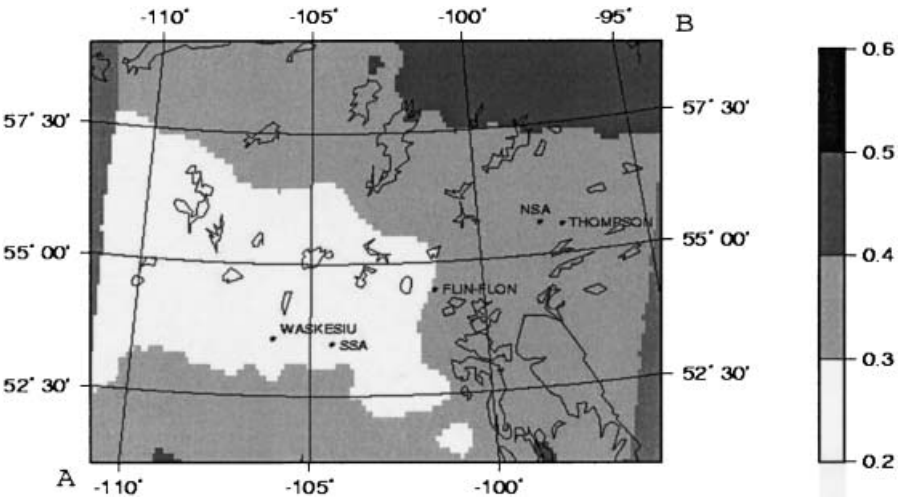

Figure 4. End of May/June/July/mid-August 1994 map of aerosol optical depth derived from NOAA-11 AVHRR channel 1 reflectance data over the BOREAS super-site.

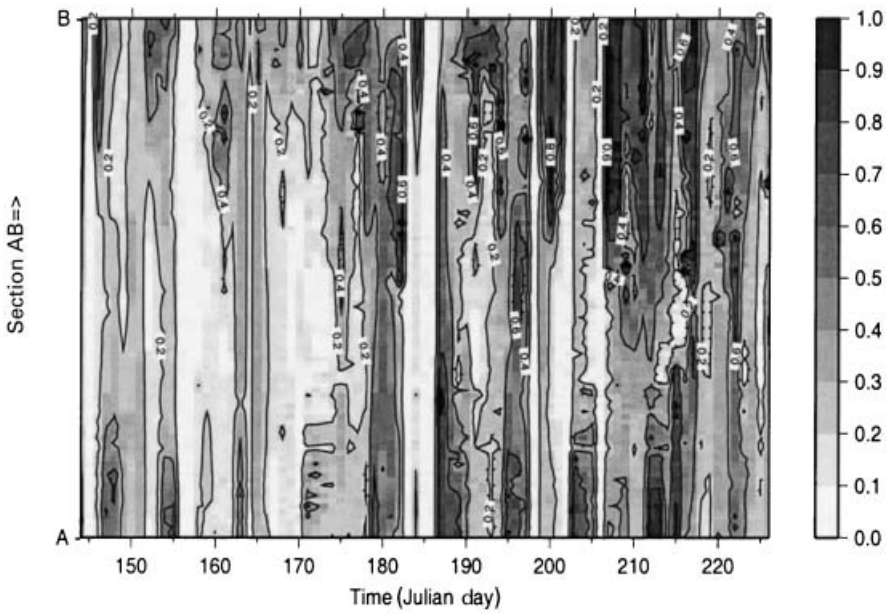

Figure 5. AOD time evolution along the section AB (as defined in figure 4) in the BOREAS super-site as retrieved from NOAA-11 AVHRR channel 1 reflectance data from 24 May to 14 August 1994.

a 10 km × 10 km resolution. Due to the sparse AOD data resolution, we get an additional file 'AOD-BOREAS94_I.gif' in which missing data were reconstructed using an interpolation method. The interpolation method we used relies on a cubic interpolation function requiring at least three retrieved AOD values and is performed inside an interpolation window of variable size centred on the mesh of the grid for which an AOD value has to be provided. When less than three retrieved AOD values are found in the interpolation window, no value is provided and the AOD is set to zero. These animations well indicate that the major source of AOD variability over the BOREAS domain is related to the occurrence of forest fires. As highlighted in figure 4, which provides a map of the averaged AOD from the end of May to mid-August 1994, these fires account for an AOD gradient over the BOREAS domain during the time period of investigation.

Figure 5 displays the AOD temporal evolution along the cross-section AB defined in figure 4 (from the lower left corner to the upper right corner). The white patterns in this figure essentially reflect the lack of AOD data due to a too sparse distribution of retrieved AOD values in the NOAA-11 AVHRR images. It is interesting to note that hotspot records (see table 2) performed on a 10-day composite basis from June to mid-August 1994 throughout Saskatchewan and Manitoba well agree with our AOD spatio-temporal characterization over the Canadian BOREAS domain. Table 2 indicates that from 1 June to 10 July, the total number of recorded hotspots in Manitoba was about twice the number recorded for Saskatchewan; parallel to that, figure 4 shows that on average the AOD was larger in Manitoba than in Saskatchewan. Finally, figure 5 indicates that, at least along the cross-section AB, the larger AOD values were found during the month of July in Manitoba as reported in the hotspot records in table 2.

Table 2. Hotspots for 10-day composite number from 1 June to 10 August 1994 recorded throughout Saskatchewan and Manitoba.

Time periods (1994)	Saskatchewan	Manitoba
1–10 June	432	144
11–20 June	34	29
21–30 June	1387	826
1–10 July	945	1157
10–20 July	454	2043
21–31 July	585	1698
1–10 August	783	3106
Total	4620	9003

5. Conclusions and perspective

In this paper we have investigated the potential of AVHRR data to characterize the spatial and temporal variation of aerosol optical depth at the regional scale (western Canada). The methodology used to retrieve aerosol optical depths was based on the dark target approach over dense vegetation and dark water scenes since this approach is, with certain constraints, sensitive to aerosols over dense boreal forest at red wavelengths. More specifically, we have shown that the detection of dark surface pixels as a basis for remote sensing of aerosol over land can benefit substantially from detection of dark pixels using their reflectivity signature in the AVHRR 3.75 μm channel. Applying the inversion algorithm to NOAA-11 AVHRR data acquired from 24 May to 14 August 1994 over the Canadian BOREAS super-site, we have shown that the major source of variability in the spatio-temporal distribution of the aerosol optical depth in the BOREAS domain during the time period of investigation was related to the occurrence of forest fires.

Comparison of the inversion results with ground data obtained from Sun photometers indicates a relatively good agreement between the retrieved and recorded aerosol optical depth values. This validation exercise has, however, highlighted two weakness in our retrieval procedure. The first is related to a thin cloud reflectance contamination. This drawback could be solved by performing an additional cloud screening before proceeding. The second source of error comes from the invariant use of a continental aerosol model which was made to compute the path radiance, the spherical albedo of the atmosphere, and the diffuse atmospheric transmittance. A way to remove this difficulty consists of the extension of our LUT to an additional aerosol model, namely a biomass burning aerosol model. The default will be to start the inversion procedure by considering the continental aerosol model and correct large retrieved aerosol optical depth values by performing an additional inversion which will then use the biomass burning aerosol model.

Finally, with these two adaptations we believe that applying our aerosol optical depth retrieval algorithm to the nearly 20 years' records of AVHRR data could be very valuable to determine the aerosol optical depth spatio-temporal dynamics over western Canada. Such a detailed analysis of the spatial and temporal behaviour of AOD at the regional scale is very useful for climate studies and for transport model validation.

Acknowledgments

The authors are grateful to Normand Bussière (Environment Canada) for NOAA-11 AVHRR data pre-processing and gridded total precipitable water content from the RFE model. We thank Norman O'Neill (CARTEL/Université de Sherbrooke) for providing hotspot data and for his constructive remarks and comments. We are also especially grateful to Eric Vermote and Nasmi El Saleous (NASA/Goddard Space Flight Center–University of Maryland) for having provided us with their algorithm to retrieve the reflectivity signature at 3.75 μm from AVHRR data and the LUT we used to invert the channel 1 AVHRR signal. This research was partly funded by the Natural Sciences and Engineering Research Council (NSERC) of Canada, the Canadian Climate Research Network (CCRN) and the Canadian Institute for Climate Studies (CICS). Cédric Bertrand was sponsored by the Quebec Ministry of Education and the Université catholique de Louvain (Belgium) for this work.

References

ACKERMAN, S. A., 1989, Using the radiative temperature difference at 3.7 and 11 μm to track dust outbreaks. *Remote Sensing of Environment*, **27**, 129–133.

BOKOYE, A. I., ROYER, A., O'NEILL, N. T., CLICHE, P., FEDOSE-JEVS, G., TEILLET, P. M., and MCARTHUR, B., 2001, Characterization of atmospheric aerosols across Canada from a ground-based sunphotometer network: AEROCAN. *Atmosphere–Ocean*, **39**, 429–456.

BUSSIÈRES, N., 2002, Thermal features of the Mackenzie Basin from NOAA AVHRR observations for summer 1994. *Atmosphere–Ocean*, **40**, 233–244.

BUSSIÈRES, N., VERSEGHY, D., and MCPHERSON, J. I., 2002, The evolution of AVHRR-derived water temperatures over boreal lakes. *Remote Sensing of Environment*, **80**, 373–384.

CIHLAR, J., CHEN, J., and LI, Z., 1997, Seasonal AVHRR multichannel data sets and products for studies of surface–atmosphere interactions. *Journal of Geophysical Research*, **102**, 29 625–29 640.

COX, C., and MUNK, W., 1954, Measurements of the roughness of the sea surface from photographs of the sun glitter. *Journal of the Optical Society of America*, **44**, 838–850.

DERRIEN, M., FARKI, B., HARANG, L., LE GLÉAU, H., NOYALET, A., POCHIC, D., and SAIROUNI, A., 1993, Automatic cloud detection applied to NOAA-11/AVHRR imagery. *Remote Sensing of Environment*, **46**, 246–267.

FRASER, R. S., FERRARE, R. A., KAUFMAN, Y. J., and MATTOO, S., 1992, Algorithm for atmospheric corrections of aircraft and satellite imagery. *International Journal of Remote Sensing*, **13**, 541–557.

HALTHORE, N. R., THOMAS, F. E., HOLBEN, B. N., and MARKHAM, B. L., 1997, Sun photometric measurements of atmospheric water vapor column abundance. *Journal of Geophysical Research*, **102**, 4343–4352.

HIGURASHI, A., NAKAJIMA, T., HOLBEN, B. N., SMIRNOV, A., FROUIN, R., and CHATENET, B., 2000, A study of global aerosol optical climatology with two-channel AVHRR remote sensing. *Journal of Climate*, **13**, 2011–2027.

HOLBEN, B. N., VERMOTE, E., KAUFMAN, Y. J., TANRÉ, D., and KALB, V., 1992, Aerosols retrieval over land from AVHRR data—application for atmospheric correction. *IEEE Transactions on Geoscience and Remote Sensing*, **30**, 212–222.

JONES, M. S., SAUNDERS, M. A., and GUYMER, T. H., 1996, Global remnant cloud contamination in the along-track scanning radiometer data: source and removal. *Journal of Geophysical Research*, **101**, 12 141–12 148.

KAUFMAN, Y. J., and REMER, L., 1994, Detection of forests using mid-IR reflectance: an application for aerosol studies. *IEEE Transactions on Geoscience and Remote Sensing*, **32**, 672–683.

KAUFMAN, Y. J., and SENDRA, C., 1988, Algorithm for automatic atmospheric corrections to visible near-IR satellite imagery. *International Journal of Remote Sensing*, **9**, 1357–1381.

KAUFMAN, Y. J., TANRÉ, D., and BOUCHER, A., 2002, A satellite view of aerosols in the climate system. *Nature*, **419**, 215–223.

KNAPP, K. R., and STOWE, L. L., 2002, Evaluating the potential for retrieving aerosol optical depth over land from AVHRR pathfinder data. *Journal of Atmospheric Science*, **59**, 279–293.

LEE, T. Y., and KAUFMAN, Y. J., 1986, Non-Lambertian effects on remote sensing of surface reflectance and vegetation index. *IEEE Transactions on Geoscience and Remote Sensing*, **24**, 699–708.

LI, Z., CIHLAR, J., ZHENG, X., MOREAU, L., and LY, H., 1996, The bidirectional effects of AVHRR measurements over boreal regions. *IEEE Transactions on Geoscience and Remote Sensing*, **34**, 1308–1322.

LI, Z., NADON, S., and CIHLAR, J., 2000, Satellite detection of Canadian boreal forest fires: development and application of an algorithm. *International Journal of Remote Sensing*, **21**, 3057–3069.

LOECHEL, S. E., WALTHALL, C. L., BROWN DE COLSTOUN, E., CHEN, J., MARKHAM, B. L., and MILLER, J., 1997, Variability of boreal forest reflectances as measured from a helicopter platform. *Journal of Geophysical Research*, **102**, 29 495–29 503.

LONDON, J., BOJKOV, R. D., OLTMANS, S., and KELLEY, J. L., 1976, Atlas of the global distribution of total ozone. July 1957–June 1967. National Center for Atmospheric Research Technical Note NCAR/TN/113+STR, NCAR, Boulder, CO, USA.

MAILHOT, J., SARRAZIN, R., BILODEAU, B., BRUNET, N., MÉTHOT, A., PELLERIN, G., CHOUINARD, C., GARAND, L., GIRARD, C., and HOGUE, R., 1995, Changes to the Canadian regional forecast system: description and evaluation of the 50-km version. *Atmosphere–Ocean*, **33**, 55–80.

MASUDA, K., TAKASHIMA, T., and TAKAYAMA, Y., 1988, Emissivity of pure and sea waters for the model surface in the infrared window regions. *Remote Sensing of Environment*, **24**, 313–329.

O'NEILL, N. T., ECK, T. F., HOLBEN, B. N., SMIRNOV, A., ROYER, A., and LI, Z., 2002, Optical properties of boreal forest fire smoke derived from sunphotometry. *Journal of Geophysical Research*, **107**, D11, 10.1029/001JD000877.

ROGER, J. C., and VERMOTE, E. F., 1998, A method to retrieve the reflectivity signature at 3.75 μm from AVHRR data. *Remote Sensing of Environment*, **64**, 103–114.

SELLERS, P., HALL, F. G., KELLY, R. D., BLACK, A., BALDOUCHI, D., BERRY, J., RYAN, M., RANSON, K. J., CRILL, P. M., LETTENMAIER, D. P., MARGOLIS, H., CIHLAR, J., NEWCOMER, J., FITZJARROLD, D., JARVIS, P. G., GOWER, S. T., HALLIWELL, D., WILLIAMS, D., GOODISON, B., WICKLAND, D. E., and GUERTIN, F. E., 1995, The BOReal Ecosystem–Atmosphere Study (BOREAS): an overview and early results from the 1994 field year. *Bulletin of the American Meteorological Society*, **76**, 1549–1577.

SOBRINO, J. A., COLL, C., and CASELLES, V., 1991, Atmospheric correction for land surface temperature using NOAA-11 AVHRR Channels 4 and 5. *Remote Sensing of Environment*, **38**, 19–34.

SOUFFLET, V., TANRÉ, D., ROYER, A., and O'NEILL, N. T., 1997, Remote sensing of aerosols over boreal forest and lakes from NOAA/AVHRR data. *Remote Sensing of Environment*, **60**, 22–34.

STOWE, L. L., JACOBOWITZ, H., OHRING, G., KNAPP, K., and NALLI, N., 2002, The AVHRR pathfinder atmosphere (PATMOS) data set: initial analyses and evaluations. *Journal of Climate*, **15**, 1243–1260.

TORRES, O., BHARTIA, P. K., HERMAN, J. R., AHMAD, Z., and GLEASON, J., 1998, Derivation of aerosol properties from satellite measurements of backscattered ultraviolet radiation: theoretical basis. *Journal of Geophysical Research*, **103**, 17 099–17 110.

VAN DE GRIEND, A. A., and OWE, M., 1993, On the relationship between thermal emissivity and the normalized difference vegetation index for natural surfaces. *International Journal of Remote Sensing*, **14**, 1119–1131.

VERMOTE, E. F., and TANRÉ, D., 1992, Analytical expressions for radiative properties of planar Rayleigh scattering media including polarization contribution. *Journal of Quantitative Spectroscopy and Radiative Transfer*, **47**, 305–314.

VERMOTE, E. F., and VERMEULEN, A., 1999, Atmospheric correction algorithm: spectral

reflectances (MOD09). MODIS Algorithm Technical Background Document, 107 pp. http://modis-land.gsfc.nasa.gov/pdfs/atbd_mod08.pdf

VERMOTE, E. F., TANRÉ, D., DEUZE, J. L., HERMAN, M., and MORCRETTE, J. J., 1997a, Second simulation of the satellite signal in the solar spectrum: an overview. *IEEE Transactions on Geoscience and Remote Sensing*, **35**, 675–687.

VERMOTE, E. F., EL SALEOUS, N., JUSTICE, C. O., KAUFMAN, Y. J., PRIVETTE, J. L., REMER, L., ROGER, J. C., and TANRÉ, D., 1997b, Atmospheric correction of visible to middle-infrared EOS–MODIS data over land surfaces: background, operational algorithm and validation. *Journal of Geophysical Research*, **102**, 17 131–17 141.

WORLD METEOROLOGICAL ORGANIZATION (WMO), 1986, World Climate Programme (WCP)-112, A preliminary cloudless standard atmosphere for radiation computation. World Meteorological Organization, WMO/TD–No. 24, Geneva, Switzerland.